J Mater Sci (2022) 57:11523–11536

Chemical routes to materials

In situ polymerization synthesis of polyaniline/strontium niobate nanocomposite for highly sensitive electrochemical detection of catechol

Zi-Chun Fan[1], Xian-Yong Wei[1,2,*], Zhi-Wei Tong[3,*], Hao-Ran Wang[3], and Zhi-Min Zong[1]

[1] *Jiangsu Province Engineering Research Center of Fine Utilization of Carbon Resources, China University of Mining and Technology, Xuzhou 221116, Jiangsu, China*

[2] *State Key Laboratory of High-Efficiency Utilization and Green Chemical Engineering, Ningxia University, Yinchuan 750021, Ningxia, China*

[3] *Jiangsu Key Laboratory of Function Control Technology for Advanced Materials, School of Environmental and Chemical Engineering, Jiangsu Ocean University, Lianyungang 222005, Jiangsu, China*

Received: 29 January 2022
Accepted: 7 May 2022
Published online: 11 June 2022

ABSTRACT

Catechol shows a wide range of applications in real life, but it has been considered as an organic pollutant due to its potential harm to the ecological environment and human health, so the monitoring of catechol is particularly important. In this work, an electrochemical sensor for the detection of catechol was developed based on an organic/inorganic layered nanocomposite polyaniline/strontium niobate (PANI/$HSr_2Nb_3O_{10}$) synthesized by in situ polymerization. Some characterization methods such as X-ray diffraction patterns, scanning electron microscope, high-resolution transmission electron microscope, X-ray photoelectron spectroscopy and Fourier-transform infrared spectroscopy were systematically used to evaluate the structure, composition, and morphology of the as-prepared samples. Compared with other single component modified electrodes, PANI/$HSr_2Nb_3O_{10}$/GCE can accelerate the electron transfer ability and possess larger electroactive surface area due to the synergistic effect of PANI and $HSr_2Nb_3O_{10}$, which resulted in enhanced electrocatalytic activity toward catechol. A pair of well-defined redox peaks observed on PANI/$HSr_2Nb_3O_{10}$/GCE correspond to the redox process of catechol, the mechanism of which is a reversible conversion between catechol and quinone. Under optimized conditions, the differential pulse voltammetry was performed for the detection of catechol, and the detection limit of 0.02 μM was obtained in the concentration range of 0.025–4.97 mM. Additionally, the developed electrochemical sensor also exhibits satisfied repeatability, long-term

Handling Editor: Dale Huber.

Address correspondence to E-mail: wei_xianyong@163.com; zhiweitong575@hotmail.com
E-mail Addresses: zichunfan@hotmail.com; wanghaoran163@outlook.com; zong_zhimin@163.com

https://doi.org/10.1007/s10853-022-07319-0

stability, reproducibility, and anti-interference and shows practicality in environmental water samples, which further reveals the feasibility of the sensor for practical applications.

Introduction

Catechol (1,2-dihydroxybenzene), as an important phenolic compound, has widespread used in several fields such as dyes, paper, cosmetics, plastics, synthetic fibers, textiles, agricultural chemicals, and pharmaceuticals [1–4]. In the process of application, catechol has been recognized as a kind of harmful organic contaminant because its high toxicity cripples the health of many biological species, and low degradability menaces the sustainable development of ecological environment [5, 6]. This has attracted worldwide attention. The emission standard (GB 8978-1996) of China for phenolic compounds is 0.5 mg mL^{-1} [7]. The U.S. Environmental Protection Agency (EPA) and the European Union (EU) have included it in the list of primary environmental pollutant to be monitored [8]. Therefore, it is very critical to monitor catechol qualitative and quantitative for human health and ecological environment. Nowadays, various analytical techniques have been developed to detect the catechol, such as synchronous fluorescence [9], gas chromatography [10], spectrophotometry [11], chemiluminescence [12], and electrochemical methods [13, 14]. Compared with other techniques, electrochemical methods stand out due to their merits of economical instrumentation, high sensitivity, fast response, easy operation, facilitation for real-time on-site analysis, and time-saving and have a wide range of applicability in agriculture, industrial food, environmental and clinical analysis [15–18]. Additionally, it is hard to directly detect catechol with conventional working electrodes owing to the poor current response and fouling on the electrode surface [8]. Hence, a novel electrode material designed to detect catechol sensitively is urgently needed.

Recently, organic–inorganic nanocomposites have focused on much attention because of superior optical, mechanical, electrical, dielectric, magnetic, and photocatalytic properties [19]. Specially, organic–inorganic nanocomposites composed of organic polymers and inorganic nanoparticles express as a new type of materials with significantly enhanced performances when compared with their individual component [20]. Polyaniline (PANI), a sort of conducting electroactive polymer, has presented advantageous redox properties, high conductivity, cost-effectiveness, environmental stability, and simple synthesis process and has exhibited acceptable potential application in electrochemical sensors, conductive fibers, and batteries [21, 22]. Figure 1 shows the basic structure of PANI (y = 0, 0.5, 1), which possesses stable heterocyclic aromatic backbone and functionality-rich skeleton and can be used to fabricate multifunctional nanocomposites [23]. Moreover, the prominent redox behavior of PANI and its ability to regulate the transfer of electrons between the electrode surface and the reaction site make it a promising electrode material for the development of electrochemical sensors [24]. As a result, some polyaniline-based nanocomposites such as BC/clay/PANI, polyaniline/graphene, $ZrSiO_4$@-NPANI@nZVCu, polyaniline/zinc bismuthate, SnO_2/PANI/Pd have been widely used in aerogels, electrochemical sensors, nanocatalyst, gas sensors and other fields [25–29]. In the field of inorganic materials, two-dimensional layered metal oxide semiconductors (LMOSs) have drawn extensive attention owing to some superior properties of unique layered structure, electrical conductivity, large surface area and ion-exchange capacity [30]. The stability of LMOSs has led to the development of several intercalation techniques to synthesize organic–inorganic nanocomposites based on LMOSs for electrochemical applications, such as MB-$Ca_2Nb_3O_{10}$ [31], Fe^{III}TMPyP-Nb_3O_8 [32], and Li/RGO-MnO_2 [33]. $KSr_2Nb_3O_{10}$, as a typical LMOS, has the outstanding characteristics of LMOS and was selected as the base material in this work. Herein, a hypothesis was proposed to combine the excellent properties of conductive polymer PANI with the unique features of $KSr_2Nb_3O_{10}$, resulting in producing a synergistic effect of these two materials.

In this work, the organic–inorganic layered nanocomposite PANI/$HSr_2Nb_3O_{10}$ was constructed by inserting aniline (ANI) molecules into the

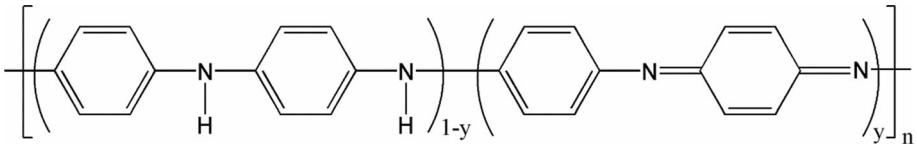

Figure 1 The basic structure of PANI.

interlayer of $HSr_2Nb_3O_{10}$ and then polymerizing the interlaminar ANI molecules by in situ polymerization. Thereafter, a novel electrochemical sensor based on the PANI/$HSr_2Nb_3O_{10}$ nanocomposite was designed for the detection of catechol. The performance of the sensor was studied by cyclic voltammetry (CV) and differential pulse voltammetry (DPV). The analytical results illustrate that the sensor combined with unique properties of PANI and $HSr_2Nb_3O_{10}$ exhibited good current response and electrocatalytic activity in the process of detecting catechol.

Experimental

Materials and reagents

Potassium carbonate (K_2CO_3), strontium carbonate (Sr_2CO_3), niobium (V) oxide (Nb_2O_5), and hydrochloric acid (HCl) were bought from Sinopharm Chemical Reagent Co., Ltd (China). CC was acquired from Shanghai Aladdin Biochemical Technology Co., Ltd (China). Sodium dihydrogen phosphate dihydrate ($NaH_2PO_4{\cdot}2H_2O$) and disodium hydrogen phosphate dodecahydrate ($Na_2HPO_4{\cdot}12H_2O$) were purchased from Xilong Scientific Co., Ltd (Guangdong, China). All chemicals and reagents were used without further purification.

Fabrication of PANI/$HSr_2Nb_3O_{10}$ nanocomposite

The layered host material of $KSr_2Nb_3O_{10}$ was synthesized by calcination of the mixture of K_2CO_3, Sr_2CO_3 and Nb_2O_5 in molar ratio of 1.1:4:3 at 1150 °C for 24 h [34]. The resulting $KSr_2Nb_3O_{10}$ (1 g) was dispersed in 6 M HCl (30 mL) aqueous solution and stirred at room temperature for three days to obtain the protonated product $HSr_2Nb_3O_{10}$. Notably, the fresh HCl was replaced once a day during the proton exchange reaction. The mixed solution was centrifuged at 8000 r min^{-1} for five minutes and washed with distilled water for several times, and then, the obtained $HSr_2Nb_3O_{10}$ was dried at 60 °C in the vacuum oven overnight and stored away.

To prepare the PANI/$HSr_2Nb_3O_{10}$ nanocomposite, $HSr_2Nb_3O_{10}$ (1 g) was first dissolved in a round-bottom flask with 20 mL distilled water, and then, 3 mL ANI was added to the suspension as well. Herein, the ANI used in the reaction is a newly distilled ANI. The reaction mixture was stirred vigorously at room temperature and carried out in a nitrogen atmosphere. Finally, the suspension was centrifuged and washed with distilled water for three times and then dried at 50 °C in the vacuum oven for 24 h. The harvested white powder was ANI/$HSr_2Nb_3O_{10}$.

0.5 g of ANI/$HSr_2Nb_3O_{10}$ was dispersed in a mixture containing 0.1 M HCl and 1 M $(NH_4)_2S_2O_8$. Then, the mixed solution was stirred at 50 °C for three days. During the in situ polymerization, the color of the sample changed from white through mazarine to dark gray. After the completion of polymerization, the precipitate was centrifuged and washed several times and dried at 50 °C overnight. The final nanocomposite was named as PANI/$HSr_2Nb_3O_{10}$.

Preparation of PANI/$HSr_2Nb_3O_{10}$/GCE

2 mg PANI/$HSr_2Nb_3O_{10}$ nanocomposite was dispersed into 1 mL distilled water and sonicated for two hours. The obtained homogeneous suspension was dripped onto the polished glassy carbon electrode (GCE) by a drip-coating method. The modified GCE is denoted as PANI/$HSr_2Nb_3O_{10}$/GCE. A schematic illustration of fabrication process of PANI/$HSr_2Nb_3O_{10}$/GCE electrochemical sensor is shown in Fig. 2.

Characterization

X-ray diffraction (XRD) data were obtained by a RINT 2000 diffractometer (Cu Kα radiation, λ = 0.154 nm, Rigaku) with 2θ from 1.5° to 70°. Scanning electron micrograph (SEM) and transmission electron microscope (TEM) images were

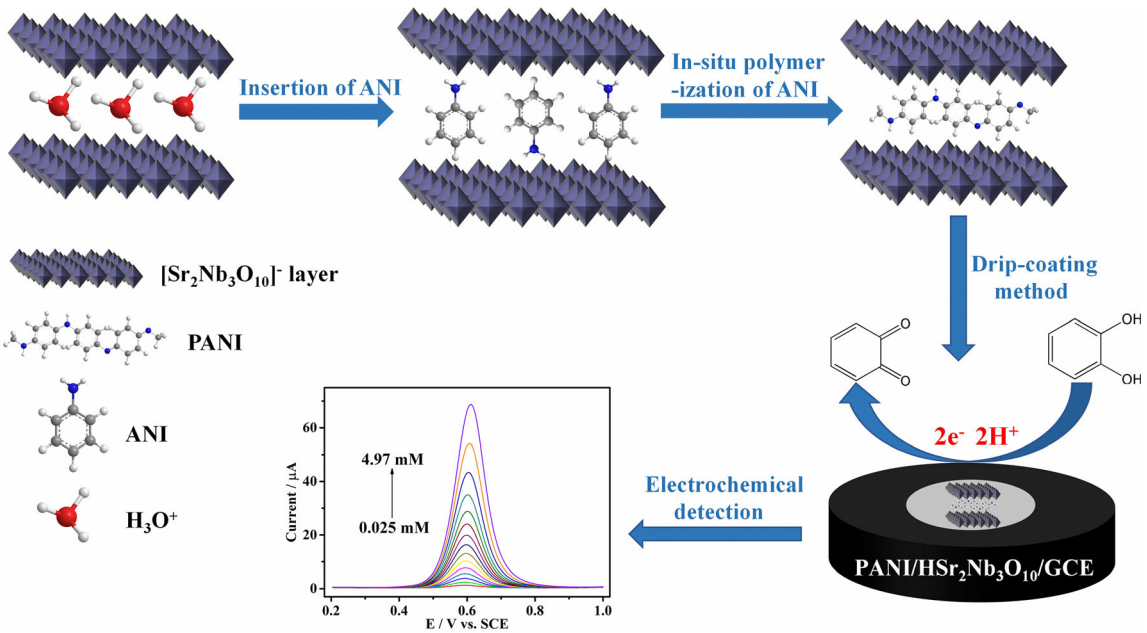

Figure 2 Schematic illustration of fabrication process of PANI/$HSr_2Nb_3O_{10}$/GCE electrochemical sensor for detection of catechol.

obtained by a JSM-5600 apparatus working at 15 kV for the samples. The elemental composition of PANI/$HSr_2Nb_3O_{10}$ nanocomposite was investigated by a high-angle annular dark-field scanning transmission electron microscope (HAADF-STEM). X-ray photoelectron spectroscopy (XPS) data were performed from an ESCALAB 250Xi spectrometer. Fourier-transform infrared spectra (FTIR) were collected on a Shimadzu FTIR-8400S spectrometer. Thermal gravimetric/differential scanning calorimetry (TG/DSC) analysis was recorded on a Shimadzu DTG-60 apparatus from room temperature to 900 °C in nitrogen atmosphere. Electrochemical results were obtained by a CHI660C electrochemical workstation with three-electrode system. The platinum wire, saturated calomel electrode (SCE) and the PANI/$HSr_2Nb_3O_{10}$/GCE were used as the counter electrode, reference electrode and working electrode, respectively.

Results and discussion

XRD analysis

The XRD patterns of $KSr_2Nb_3O_{10}$, $HSr_2Nb_3O_{10}$, ANI/$HSr_2Nb_3O_{10}$ and PANI/$HSr_2Nb_3O_{10}$ are shown in Fig. 3. It can be clearly seen that the $KSr_2Nb_3O_{10}$ and $HSr_2Nb_3O_{10}$ have strong and sharp diffraction peaks,

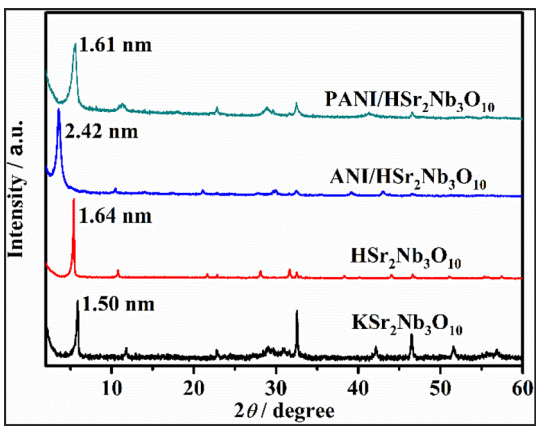

Figure 3 XRD patterns of $KSr_2Nb_3O_{10}$, $HSr_2Nb_3O_{10}$, ANI/$HSr_2Nb_3O_{10}$ and PANI/$HSr_2Nb_3O_{10}$.

demonstrating their well crystallinity. However, the crystallinities of the ANI/$HSr_2Nb_3O_{10}$ and PANI/$HSr_2Nb_3O_{10}$ nanocomposite are relatively poor. The XRD pattern of calcined $KSr_2Nb_3O_{10}$ matches well with the previous literature [35]. A sharp (002) diffraction peak of the original $KSr_2Nb_3O_{10}$ can be observed at 5.88°. According to Bragg's Law, the basal spacing (d_{002}) of $KSr_2Nb_3O_{10}$ is calculated as 1.50 nm. Through acidification process, the (002) diffraction peak of $HSr_2Nb_3O_{10}$ shifts to a lower angle (5.38°), and the basal spacing of $HSr_2Nb_3O_{10}$ increases to 1.64 nm. It means that the interlayer distance is enlarged because of the replacement of K^+ by H_3O^+

after the protonation. The shift of the (002) diffraction peak of ANI/$HSr_2Nb_3O_{10}$ to a lower 2θ angle (3.61°) because the amino group (–NH_2) on the benzene ring reacts with the hydrogen proton in the interlayer to generate –NH_3^+. In addition, the (002) diffraction peak of PANI/$HSr_2Nb_3O_{10}$ at 5.44° is ascribed to the formation of PANI by in situ polymerization of ANI. As the polymerization progressed, the interlayer spacing began to decrease, possibly due to the chemical bonding of ANI molecules [36]. The basal spacing (d) and interlayer spacing (Δd) values of the samples are listed in Table 1. The thickness of $[Sr_2Nb_3O_{10}]^-$ slab (1.26 nm) can be obtained by subtracting the diameter of the K^+ cation (0.24 nm) [37]. Thereby, the Δd values of ANI/$HSr_2Nb_3O_{10}$ and PANI/$HSr_2Nb_3O_{10}$ are calculated as 1.16 and 0.35 nm, respectively. In consideration of the molecule length of ANI (0.7 nm) [38], it can be inferred that ANI molecules form a monolayer in the interlayer of $[Sr_2Nb_3O_{10}]^-$ nanosheets.

Morphology analysis

The morphologies and structures of the obtained samples were confirmed by SEM. As exhibited in Fig. 4a–d, the smooth surface and layered structure of the original $KSr_2Nb_3O_{10}$ can be clearly observed. After the proton exchange process, the structure of $HSr_2Nb_3O_{10}$ is essentially the same as the original material. With the intercalation of ANI, the surface, and edges of the ANI/$HSr_2Nb_3O_{10}$ become rough and irregular. Through in situ polymerization reaction, the laminates of PANI/$HSr_2Nb_3O_{10}$ become smaller and agglomerate together, but remain the layered structure. From Fig. 4e, it can be determined that the size of PANI/$HSr_2Nb_3O_{10}$ nanocomposite is within the range of several hundred nanometers by TEM. In HRTEM image of nanocomposite (Fig. 4f), the spacing between the two red labeled laminates is 0.35 nm, which is consistent with the result of XRD. Additionally, the element composition of PANI/$HSr_2Nb_3O_{10}$ nanocomposite was analyzed by HAADF-STEM in Fig. 4g–m. The elemental mapping images illustrate that the PANI/$HSr_2Nb_3O_{10}$ nanocomposite is composed of C, N, O, Sr and Nb elements with well spatial distribution, in which elements C and N are ascribed to PANI, and elements O, Sr and Nb are assigned to $HSr_2Nb_3O_{10}$, verifying the successful preparation of the nanocomposite.

Table 1 XRD data of the different samples

Compound	2θ/°	d/nm	Δd/nm
$KSr_2Nb_3O_{10}$	5.88	1.50	–
$HSr_2Nb_3O_{10}$	5.38	1.64	0.38
ANI/$HSr_2Nb_3O_{10}$	3.61	2.42	1.16
PANI/$HSr_2Nb_3O_{10}$	5.44	1.61	0.35

XPS analysis

The surface chemical composition and valence states of elements in PANI/$HSr_2Nb_3O_{10}$ nanocomposite were examined by the XPS measurements. As displayed in Fig. 5a, the survey spectrum of PANI/$HSr_2Nb_3O_{10}$ nanocomposite confirms the existence of O, N, C, Nb, and Sr elements, which is consistent with the results of elemental mapping images. For the Sr 3d spectrum in Fig. 5b, the binding energy peaks observed at 133 and 134.7 eV are attributed to $3d_{5/2}$ and $3d_{3/2}$ of Sr, respectively, indicating the presence of + 2 oxidation state of Sr element in the nanocomposite [39]. From image of Fig. 5c, two peaks at 207.1 and 209.9 eV are assigned to Nb $3d_{5/2}$ and Nb $3d_{3/2}$, respectively, which is ascribed to + 5 oxidation state of Nb element [40]. The XPS spectrum of N 1 s (Fig. 5d) shows three characteristic peaks for PANI/$HSr_2Nb_3O_{10}$. The strong peak at 399.8 eV and the weak peaks at 395.2 and 401.3 eV are, respectively, classified as the amine N, imine N, and positively charged N [41]. XPS measurement results combined with XRD and element mapping images analysis further prove the successful preparation of the nanocomposite.

IR and thermogravimetric analysis

The IR spectra of $KSr_2Nb_3O_{10}$, PANI and PANI/$HSr_2Nb_3O_{10}$ are presented in Fig. S1a. The characteristic bands of $KSr_2Nb_3O_{10}$ at 924 and 584 cm^{-1} are attributed to the stretching vibration of Nb–O [42]. Similarly, these absorption bands also appear in polymerized product. For PANI/$HSr_2Nb_3O_{10}$, some characteristic bands belonging to PANI can be observed at 1638 cm^{-1} [υ(C=N)], 1489, 1392 cm^{-1} [benzenoid ring υ(C=C)], 1322 cm^{-1} [υ(C–N)] and 1131 cm^{-1} [υ(C–H)] [43]. The results confirm the existence of PANI in the PANI/$HSr_2Nb_3O_{10}$ nanocomposite.

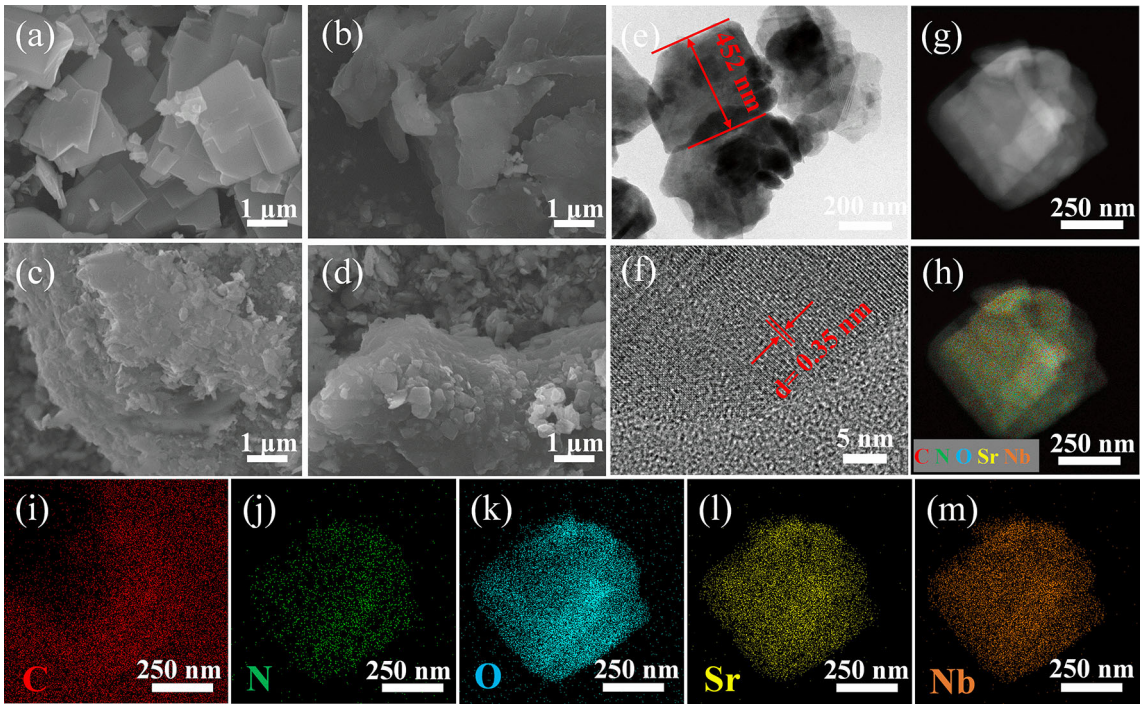

Figure 4 SEM images of **a** $KSr_2Nb_3O_{10}$, **b** $HSr_2Nb_3O_{10}$, **c** ANI/$HSr_2Nb_3O_{10}$ and **d** PANI/$HSr_2Nb_3O_{10}$; **e** TEM, **f** HRTEM, **g** HAADF-STEM and **h**–**m** Elemental mapping images of PANI/$HSr_2Nb_3O_{10}$ nanocomposite.

Figure 5 **a** XPS survey spectrum of PANI/$HSr_2Nb_3O_{10}$ nanocomposite; XPS spectra of **b** Sr 3d, **c** Nb 3d, and **d** N 1 s.

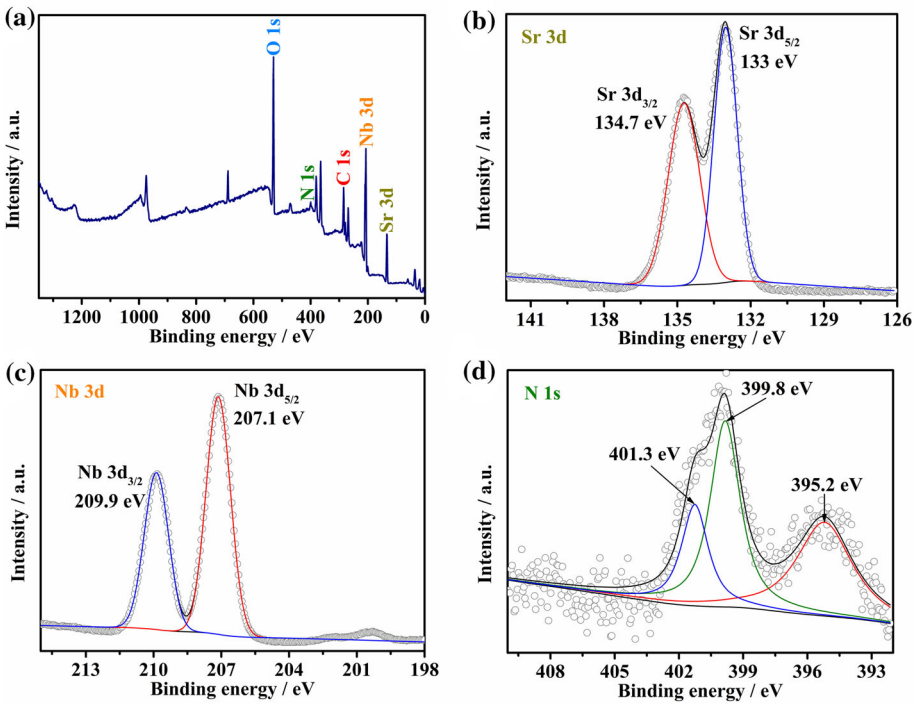

The weight loss of $KSr_2Nb_3O_{10}$ and PANI/$HSr_2Nb_3O_{10}$ nanocomposite in the range of room temperature to 900 °C was identified by TG/DSC curves. As shown in Fig. S1b, the thermal behavior of PANI/$HSr_2Nb_3O_{10}$ nanocomposite shows three-step weight loss process. Briefly, the three steps are divided into 25–100 °C, 100–535 °C and 535–900 °C. The corresponding thermal weightlessness processes are

assigned to the vaporization of water, elimination of HCl and decomposition of PANI, respectively. Furthermore, the exothermic peak of PANI/$HSr_2Nb_3O_{10}$ nanocomposite appears at 809 °C, which is much higher than pure PANI (530 °C) [44]. This result demonstrates that the PANI/$HSr_2Nb_3O_{10}$ nanocomposite has higher thermal stability.

Electrochemical characterization of the modified GCEs

Electrochemical impedance spectroscopy (EIS) was adopted to compare the electron transfer properties of different modified GCEs. The Nyquist plot of bare electrode, $KSr_2Nb_3O_{10}$/GCE, and PANI/$HSr_2Nb_3O_{10}$/GCE in 0.5 mM $K_3[Fe(CN)_6]$ and 0.5 mM $K_4[Fe(CN)_6]$ containing 0.1 M KCl with frequency range of 1 to 10^5 Hz is presented in Fig. 6a. The Nyquist diagram consists of a low-frequency linear part and a high-frequency semicircle part, which are attributed to the linear diffusion control process and the electron transfer resistance (Rct), respectively. The Nyquist plot of PANI/$HSr_2Nb_3O_{10}$/GCE shows the smallest Rct than other modified GCEs, illustrating greater conductivity and faster electron transfer capability. Under the same condition, the electrochemical performance of the electrode was measured by CV technique. As shown in Fig. 6b, all modified GCEs exhibit a pair of well-defined redox peaks, and the highest redox current response is observed on PANI/$HSr_2Nb_3O_{10}$/GCE. Meanwhile, the peak-to-peak separation value (ΔE_p = 0.203 V) of PANI/$HSr_2Nb_3O_{10}$/GCE is lower than bare electrode (ΔE_p = 0.403 V) and $KSr_2Nb_3O_{10}$/GCE (ΔE_p = 0.497 V). These electrochemical behaviors further confirm the great catalytic activity of PANI/$HSr_2Nb_3O_{10}$/GCE and can accelerate electron transfer.

In Fig. S2, the electrochemical active surface areas of bare electrode, $KSr_2Nb_3O_{10}$/GCE, and PANI/$HSr_2Nb_3O_{10}$/GCE were examined by CV technique in 0.5 mM $[Fe(CN)_6]^{3-/4-}$ containing 0.1 M KCl at different scan rates. For a reversible redox reaction, the following Randles–Sevcik equation can be used [45]:

$$I_p = 2.69 \times 10^5 \times D^{1/2} \times A \times v^{1/2} \times n^{3/2} \times C$$

where I_p represents the peak current, D is the diffusion coefficient of $[Fe(CN)_6]^{3-/4-}$ (1×10^{-5} cm^2 s^{-1}), A refers to the surface area of the electrode, v is the scan rate (mV s^{-1}), n is the number of electron transferred (n = 1), and C is the concentration of $[Fe(CN)_6]^{3-/4-}$ (0.5 mM). The electrochemical active surface areas of bare electrode, $KSr_2Nb_3O_{10}$/GCE, and PANI/$HSr_2Nb_3O_{10}$/GCE were calculated as 0.0019, 0.0017, and 0.0026 cm^2, respectively. PANI/$HSr_2Nb_3O_{10}$/GCE exhibits a larger active area, indicating that the prepared nanocomposite can greatly increase the effective area of the GCE.

Electrochemical behavior of PANI/$HSr_2Nb_3O_{10}$/GCE

Figure 7a shows the CV curves of PANI/$HSr_2Nb_3O_{10}$/GCE at different scan rates in 0.1 M HCl solution. The modified electrode exhibits good redox activity in the acid solution. The redox reaction mechanism is illustrated in Scheme 1 [24]. Specifically, the redox peak at − 0.14 V is due to the transition from a complete reduced leucoemeraldine state to a semi-oxidized emeraldine state. Another redox peak (0.08 V) is assigned to the conversion of emeraldine state to fully oxidized pernigraniline state [46]. With the increase of the scan rate, the anodic and cathodic peaks shift slightly to the positive and negative directions, respectively. Besides, the redox

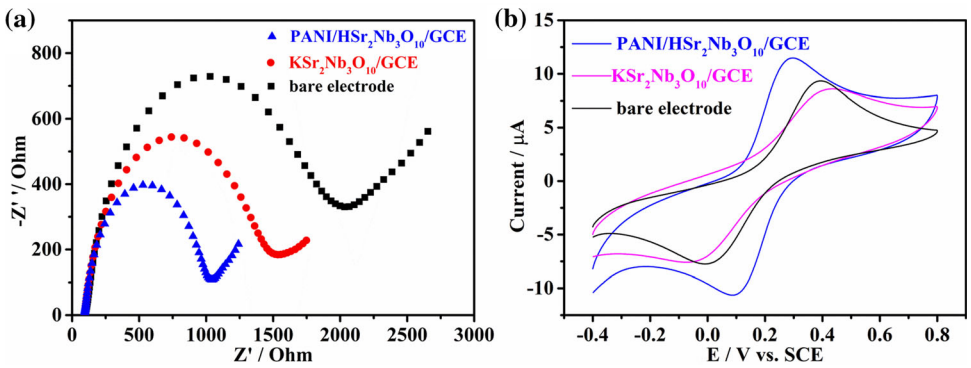

Figure 6 **a** Nyquist plots and **b** CV curves of bare electrode, $KSr_2Nb_3O_{10}$/GCE and PANI/$HSr_2Nb_3O_{10}$/GCE in 0.5 mM $K_3[Fe(CN)_6]$ and 0.5 mM $K_4[Fe(CN)_6]$ containing 0.1 M KCl.

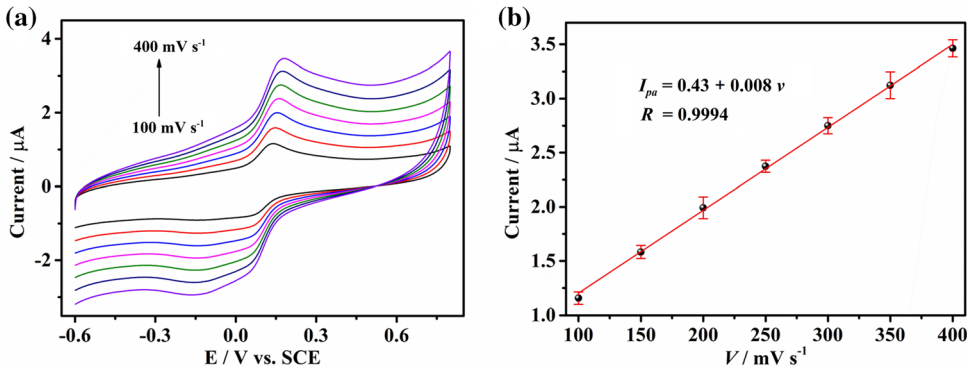

Figure 7 **a** CV curves of $PANI/HSr_2Nb_3O_{10}/GCE$ in 0.1 M HCl solution at scan rate from 100 to 400 mV s^{-1}; **b** The relationship curve between I_{pa} and v.

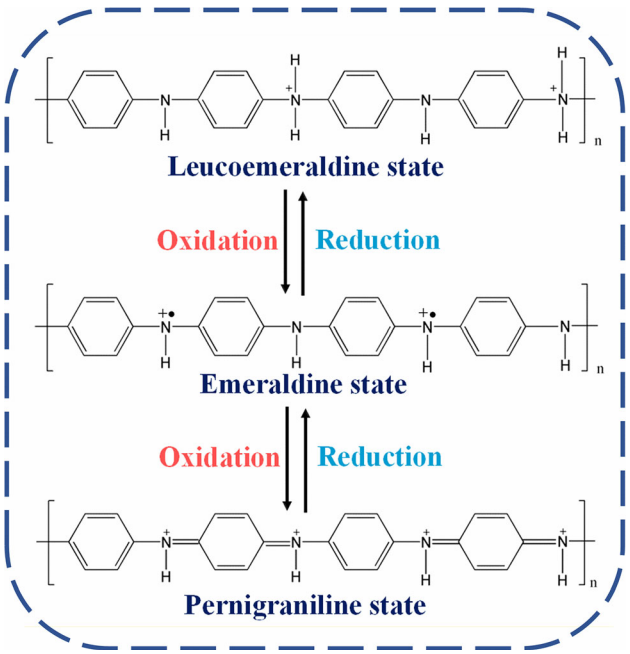

Scheme 1 The redox reaction mechanism of PANI in 0.1 M HCl.

peaks become more and more obvious, and the peak current values also increase gradually. The anodic peak current (I_{pa}) is proportional to the scan rate (v), and the linear relationship between I_{pa} and v is plotted in Fig. 7b. The linear equation can be described as I_{pa} (μA) = 0.43 + 0.008 v (mV s^{-1}) (n = 7, R = 0.9994), which illustrates that the redox reaction is a typical surface-controlled process. Here, n and R represent the number of scans and linear correlation coefficients, respectively.

Effect of pH

The influence of the pH of HCl on the electrochemical response of $PANI/HSr_2Nb_3O_{10}/GCE$ for the detection of catechol was explored by DPV technique. The plot of the response current versus different pH values (pH = 1.0, 2.0, 3.0, 4.0 and 5.0) of HCl is depicted in Fig. S3. The response current decreases with the increase of pH, and $PANI/HSr_2Nb_3O_{10}/GCE$ shows the maximum response current at pH 1.0. Hence, the HCl with pH 1.0 (the concentration is 0.1 M) was used as the optimal condition for the remaining experiments.

Electrochemical behavior of catechol at $PANI/HSr_2Nb_3O_{10}/GCE$

The individual electrocatalytic performance of catechol at different modified electrodes was evaluated using CV technique in 0.1 M HCl solution at scan rate of 100 mV s^{-1}. As given in Fig. 8, bare electrode, $KSr_2Nb_3O_{10}/GCE$, $HSr_2Nb_3O_{10}/GCE$, PANI/GCE and $PANI/HSr_2Nb_3O_{10}/GCE$ all display a pair of obvious redox peaks for catechol, indicating that the reversibility of the electron transfer process of catechol. For bare electrode, the peak-to-peak separation value (ΔE_p = 0.546 V) is the highest, and the anodic

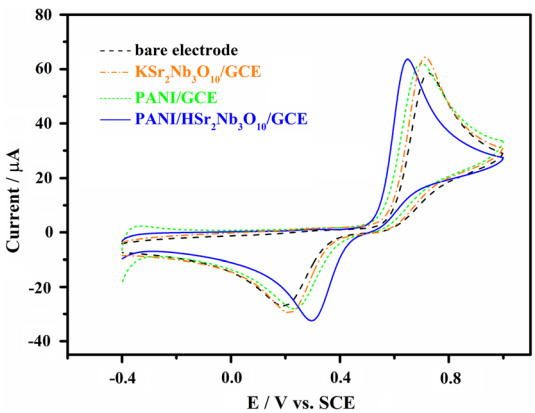

Figure 8 CV curves of bare electrode (dash line), $KSr_2Nb_3O_{10}/GCE$ (dash dot line), PANI/GCE (short dash line) and $PANI/HSr_2Nb_3O_{10}/GCE$ (solid line) in 0.1 M HCl solution containing 1.64 mM catechol at a scan rate of 100 mV s^{-1}.

and cathodic peak currents are lowest, demonstrating that the bare electrode has poor electrocatalytic performance for catechol. Moreover, the ΔE_p values of 0.501 and 0.468 V are observed at $KSr_2Nb_3O_{10}$/GCE and PANI/GCE, respectively, and the current values of the two modified electrodes are almost the same. The recorded current of PANI/$HSr_2Nb_3O_{10}$/GCE began to peak generated by the oxidation of catechol at about 0.5 V and reached the maximum peak at 0.648 V in the positive scanning. In the reverse scanning process, the reduction peak was obtained at 0.3 V, which was ascribed to a reversible conversion between catechol and quinone [45]. The probable redox reaction mechanism of catechol at PANI/$HSr_2Nb_3O_{10}$/GCE can be expressed in scheme 2 [47]. Concretely, as presented in Eq. (1), the catechol adsorbed on the surface of the modified electrode forms two hydrogen bonds with two imine hydrogen atoms on the PANI, and then, two series of single-electron transitions occur [48]. The total reaction equation can be represented as Eq. (2). Compared with the above three modified electrodes, PANI/$HSr_2Nb_3O_{10}$/GCE displays the smallest ΔE_p value (0.348 V) and highest peak current, illustrating that PANI/$HSr_2Nb_3O_{10}$/GCE possesses faster electron transfer ability and larger electroactive surface area due to the synergistic effect between PANI and $HSr_2Nb_3O_{10}$. This result suggests that PANI/$HSr_2Nb_3O_{10}$/GCE has excellent electrocatalytic performance for the detection of catechol.

Effect of scan rate

To further understand the electrochemical redox reaction kinetics of catechol, the effect of scan rate on PANI/$HSr_2Nb_3O_{10}$/GCE was investigated by CV in the potential range from − 0.4 to 1.0 V. As presented in Fig. 9a, the regular CV curves of PANI/$HSr_2Nb_3O_{10}$/GCE in 0.1 M HCl containing 1.64 mM catechol at different sweeping scan rates were clearly observed. The anodic and cathodic peak currents (I_{pa}, I_{pc}) of catechol at PANI/$HSr_2Nb_3O_{10}$/GCE increase with the increasing the scan rates and are linearly dependent on the square root of scan rate ($v^{1/2}$). Two linear relationships are depicted in Fig. 9b, and the regression equations of catechol can be represented as I_{pa} (μA) = 9.54 + 5.37 $v^{1/2}$ ($mV^{1/2}$ $s^{-1/2}$) (n = 12, R = 0.9996) and I_{pc} (μA) = − 0.74 − 3.08 $v^{1/2}$ ($mV^{1/2}$ $s^{-1/2}$) (n = 12, R = − 0.9974). These results indicate that the redox reaction of catechol at PANI/$HSr_2Nb_3O_{10}$/GCE is typical diffusion-controlled process.

Determination of catechol on PANI/$HSr_2Nb_3O_{10}$/GCE

DPV technique featured with high sensitivity and resolution has been widely employed to quantitative analysis of some biomolecules. Herein, DPV tests were carried out on PANI/$HSr_2Nb_3O_{10}$/GCE by increasing the concentration of catechol in 0.1 M HCl. From image of Fig. 9c, the response currents gradually increase and the potential values remain at about 0.6 V with the successive addition of the

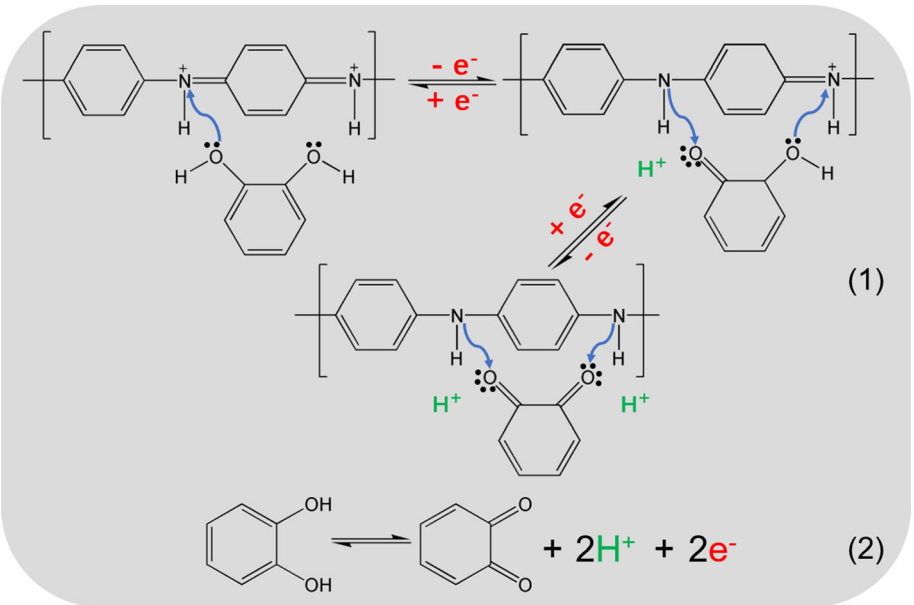

Scheme 2 The redox mechanism of catechol at PANI/$HSr_2Nb_3O_{10}$/GCE.

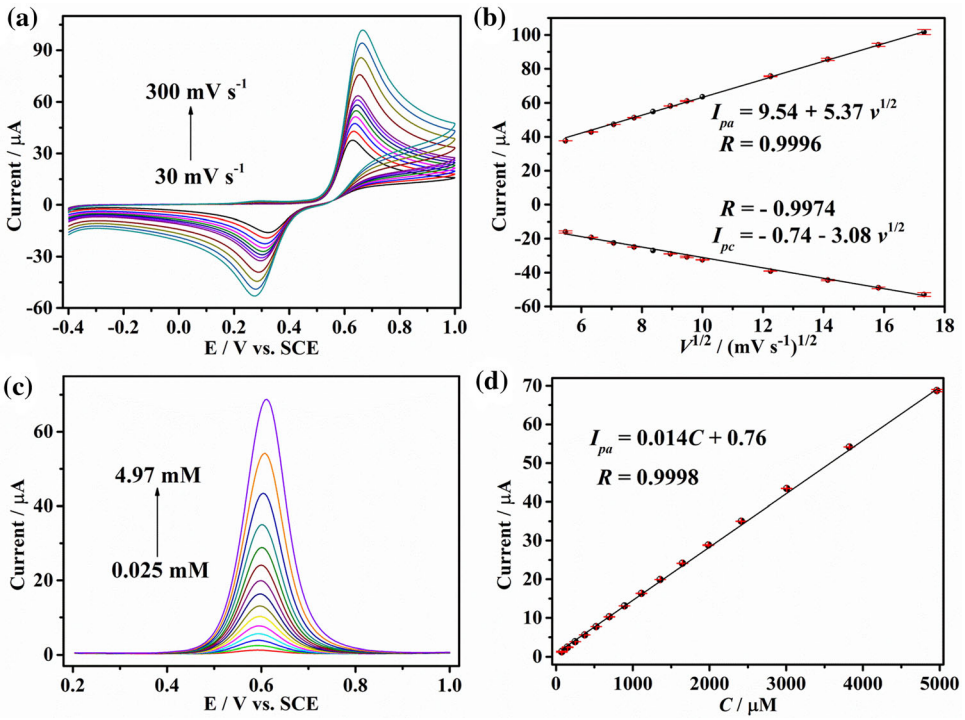

Figure 9 **a** CV curves of $PANI/HSr_2Nb_3O_{10}/GCE$ in 0.1 M HCl solution containing 1.64 mM catechol at scan rates of 30, 40, 50, 60, 70, 80, 90, 100, 150, 200, 250 and 300 mV s^{-1}; **b** the relationship curves between the I_{pa}, I_{pc} of catechol and $v^{1/2}$; **c** DPV curves of $PANI/HSr_2Nb_3O_{10}/GCE$ in 0.1 M HCl solution with different concentrations of catechol; d the relationship between I_{pa} and concentrations of catechol.

concentration of catechol. The oxidation peak current of $PANI/HSr_2Nb_3O_{10}/GCE$ is proportional to the concentration (*C*) of catechol, as illustrated in Fig. 9d. The linear equation in the different concentration intervals 0.025–4.97 mM can be expressed as I_{pa} (μA) = 0.014 *C* (μM) + 0.76 (n = 15, R = 0.9998), and the limit of detection (LOD) was calculated to be 0.02 μM at a signal-to-noise ratio of 3.0. To estimate the performance of the as-prepared $PANI/HSr_2Nb_3O_{10}/GCE$, the above analytical results are compared with some previous studies on the detection of catechol. As presented in Table 2, the obtained $PANI/HSr_2Nb_3O_{10}/GCE$ shows lower detection limit and wider linear concentration range than most other modified electrodes. Therefore, $PANI/HSr_2Nb_3O_{10}/GCE$ can be regarded as a promising electrode material for electrochemical detection of catechol.

Repeatability, stability, reproducibility, and anti-interference of $PANI/HSr_2Nb_3O_{10}/GCE$

The repeatability, stability, reproducibility, and anti-interference are significantly important parameters to evaluate the practicability and applicability of electrochemical sensor. The repeatability of $PANI/HSr_2Nb_3O_{10}/GCE$ was examined by measuring the DPV responses to 0.82 mM catechol in 0.1 M HCl. Figure 10a displays the DPV curves of fifty consecutive tests, and these curves almost completely coincident, like one curve, with the peak current and potential values basically unchanged. This indicates that $PANI/HSr_2Nb_3O_{10}/GCE$ possesses excellent

Table 2 Comparison for determination of catechol at different modified electrodes

Electrode material	Linear range (μM)	LOD (μM)	References
TACoPc/PANI/AgNPs/GCE	10–100	0.46	[49]
RGO-MWNTs/GCE	6–540	1.8	[50]
Fe_3O_4/PANI/CS/GCE	0.5–80	0.4	[51]
Co_3O_4/MWCNTs/GCE	10–800	8.5	[52]
Pyridinic-NG/GCE	5–200	1.0	[53]
Au-PdNF/rGO/GCE	3–100	0.8	[54]
AuNPs@CNCs/GCE	1–300	0.09	[55]
$PANI/HSr_2Nb_3O_{10}/GCE$	25–4970	0.02	This work

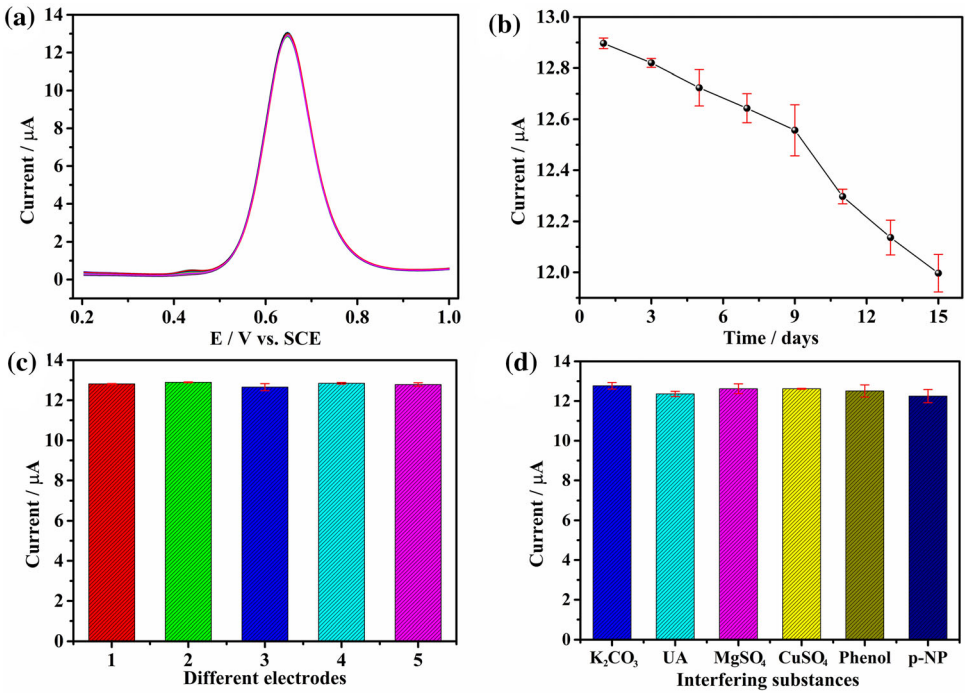

Figure 10 **a** Repeatability, **b** long-term stability and **c** reproducibility measurements of PANI/$HSr_2Nb_3O_{10}$/GCE in 0.1 HCl solution containing 0.82 mM catechol; **d** interference measurements of PANI/$HSr_2Nb_3O_{10}$/GCE with 0.76 mM catechol in the presence of 76 mM interfering substances.

repeatability. Additionally, PANI/$HSr_2Nb_3O_{10}$/GCE was stored under ambient conditions and tracked for fifteen days to explore its long-term stability. As depicted in Fig. 10b, after fifteen days, the current response maintained approximately 93.72% of the initial measured value, suggesting the good stability of PANI/$HSr_2Nb_3O_{10}$/GCE. The reproducibility was assessed from the DPV current response to catechol at five different GECs prepared independently under the same condition. Five obtained similar current values can be observed in Fig. 10c, and their relative standard deviation (RSD) was calculated as 0.58%, demonstrating the superior reproducibility of PANI/$HSr_2Nb_3O_{10}$/GCE. Figure 10d studies the anti-interference ability of PANI/$HSr_2Nb_3O_{10}$/GCE to catechol, some possible interfering substances such as K_2CO_3, uric acid (UA), $MgSO_4$, $CuSO_4$, phenol and p-Nitrophenol (p-NP) which commonly co-exist with catechol were added in the detection of catechol. In the DPV analysis of 0.76 mM catechol, the obvious current response can still be observed under the influence of interferents whose concentration is 100 times that of catechol. This illustrates the good selectivity and anti-interference of PANI/$HSr_2Nb_3O_{10}$/GCE. According to the above results, the outstanding repeatability, stability, reproducibility, and anti-interference indicate that PANI/$HSr_2Nb_3O_{10}$/GCE can be served as reliable electrochemical sensor for the detection of catechol.

Real sample analysis

To evaluate the effectiveness of the prepared electrochemical sensor in the real system, PANI/$HSr_2Nb_3O_{10}$/GCE was carried out to detect the catechol in local tap water sample by the standard addition method. As shown in Table 3, the recoveries of catechol were calculated in the range of 95.3–105.1%, and three groups of parallel experiments were recorded with the RSD values ranging from 1.1 to 3.3%. The results indicate that the proposed electrochemical sensor displays the satisfactory performance and can be used in practical applications.

Conclusion

In this work, an organic/inorganic nanocomposite PANI/$HSr_2Nb_3O_{10}$ with interesting characteristics was prepared by inserting aniline monomers into the interlayer of $HSr_2Nb_3O_{10}$, followed by in situ polymerization reaction between the layers. The successful intercalation and in situ polymerization of ANI monomers were certified by XRD, SEM, TEM, and IR. In addition, the composition of the nanocomposite

Table 3 Determination of catechol in tap water

Sample	Added (μM)	Found (μM)	Recovery (%)	RSD (%) (n = 3)
1	709	676	95.3	1.5
2	2098	2164	103.2	1.1
3	3448	3625	105.1	3.3

was further proved by the elemental analysis and XPS analysis. Based on the TG/DSC analysis, the thermally stability of PANI/$HSr_2Nb_3O_{10}$ nanocomposite was greatly improved. Under the synergistic effect of PANI and $HSr_2Nb_3O_{10}$, the electrochemical sensor constructed based on the nanocomposite displays prominent electrocatalytic performance toward catechol with the low detection limit and the wide linear concentration range. The sensor also shows good repeatability, stability, reproducibility, and anti-interference in detecting catechol. Hence, the developed PANI/$HSr_2Nb_3O_{10}$ nanocomposite can be served as an effective electrode material for detecting catechol and has potential application value in electrochemical sensor.

Acknowledgements

This work was supported by the National Natural Science Foundation of China (Grant 21776298, 22178376), the Foundation of State Key Laboratory of High-efficiency Utilization of Coal and Green Chemical Engineering (Grant 2021-K01) and the National Key Research and Development Program of China (Grant 2018YFB0604602).

Declarations

Conflict of interest The authors declare that they have no conflict of interest.

Supplementary Information: The online version contains supplementary material available at https://doi.org/10.1007/s10853-022-07319-0.

References

[1] Zhang Z, Liu J, Fan J, Wang Z, Li L (2018) Detection of catechol using an electrochemical biosensor based on engineered Escherichia coli cells that surface-display laccase. Anal Chim Acta 1009:65–72

[2] Yin D, Liu J, Bo X, Guo L (2020) Cobalt-iron selenides embedded in porous carbon nanofibers for simultaneous electrochemical detection of trace of hydroquinone, catechol and resorcinol. Anal Chim Acta 1093:35–42

[3] Yang H, Zha J, Zhang P, Qin Y, Chen T, Ye F (2017) Fabrication of $CeVO_4$ as nanozyme for facile colorimetric discrimination of hydroquinone from resorcinol and catechol. Sensor Actuat B-Chem 247:469–478

[4] Cao X, Cai X, Feng Q, Jia S, Wang N (2012) Ultrathin CdSe nanosheets: synthesis and application in simultaneous determination of catechol and hydroquinone. Anal Chim Acta 752:101–105

[5] Guo Q, Zhang M, Zhou G, Zhu L, Feng Y, Wang H, Hou H (2016) Highly sensitive simultaneous electrochemical detection of hydroquinone and catechol with three-dimensional N-doping carbon nanotube film electrode. J Electroanal Chem 760:15–23

[6] Drozd M, Pietrzak M, Pytlos J, Malinowska E (2016) Revisiting catechol derivatives as robust chromogenic hydrogen donors working in alkaline media for peroxidase mimetics. Anal Chim Acta 948:80–89

[7] Yin H, Zhang Q, Zhou Y, Ma Q, Liu T, Zhu L, Ai S (2011) Electrochemical behavior of catechol, resorcinol and hydroquinone at graphene-chitosan composite film modified glassy carbon electrode and their simultaneous determination in water samples. Electrochim Acta 56:2748–2753

[8] Radhakrishnan S, Krishnamoorthy K, Sekar C, Wilson J, Kim SJ (2015) A promising electrochemical sensing platform based on ternary composite of polyaniline-Fe_2O_3-reduced graphene oxide for sensitive hydroquinone determination. Chem Eng J 259:594–602

[9] Žiak L, Sádecká J, Májek P, Hroboňová K (2014) Simultaneous determination of phenolic acids and scopoletin in brandies using synchronous fluorescence spectrometry coupled with partial least squares. Food Anal Method 7:563–570

[10] Moldoveanu SC, Kiser M (2007) Gas chromatography/mass spectrometry versus liquid chromatography/fluorescence detection in the analysis of phenols in mainstream cigarette smoke. J Chromatogr A 1141:90–97

[11] Figueiredo EC, Tarley CRT, Kubota LT, Rath S, Arruda MAZ (2007) On-line molecularly imprinted solid phase extraction for the selective spectrophotometric determination of catechol. Microchem J 85:290–296

[12] Lu Q, Hu H, Wu Y, Chen S, Yuan D, Yuan R (2014) An electrogenerated chemiluminescence sensor based on gold nanoparticles@C60 hybrid for the determination of phenolic compounds. Biosens Bioelectron 60:325–331

[13] Ilager D, Shetti NP, Reddy KR, Tuwar SM, Aminabhavi TM (2022) Nanostructured graphitic carbon nitride (g-C_3N_4)-CTAB modified electrode for the highly sensitive detection of amino-triazole and linuron herbicides. Environ Res 204:111856

[14] Prabhu K, Malode SJ, Shetti NP, Kulkarni RM (2022) Analysis of herbicide and its applications through a sensitive electrochemical technique based on MWCNTs/ZnO/CPE fabricated sensor. Chemosphere 287:132086

[15] Ali MR, Bacchu MS, Al-Mamun MR, Rahman MM, Ahommed MS, Aly MAS, Khan MZH (2021) Sensitive MWCNT/P-Cys@ MIP sensor for selective electrochemical detection of ceftizoxime. J Mater Sci 56:12803–12813. https://doi.org/10.1007/s10853-021-06115-6

[16] Manasa G, Mascarenhas RJ, Bhakta AK, Mekhalif Z (2021) Nano-graphene-platelet/Brilliant-green composite coated carbon paste electrode interface for electrocatalytic oxidation of flavanone Hesperidin. Microchem J 160:105768

[17] Manasa G, Mascarenhas RJ, Bhakta AK, Mekhalif Z (2020) MWCNT/Nileblue heterostructured composite electrode for flavanone naringenin quantification in fruit juices. Electroanal 32:939–948

[18] Manasa G, Mascarenhas RJ, Basavaraja BM (2019) Sensitively-selective determination of Propyl Paraben preservative based on synergistic effects of polyaniline-zinc-oxide nanocomposite incorporated into graphite paste electrode. Colloid Surface B 184:110529

[19] Jiang B, Pang X, Li B, Lin Z (2015) Organic-inorganic nanocomposites via placing monodisperse ferroelectric nanocrystals in direct and permanent contact with ferroelectric polymers. J Am Chem Soc 137:11760–11767

[20] Jeon IY, Baek JB (2010) Nanocomposites derived from polymers and inorganic nanoparticles. Mater 3:3654–3674

[21] Wei WF, Cui XW, Chen WX, Ivey DG (2011) Manganese oxide-based materials as electrochemical supercapacitor electrodes. Chem Soc Rev 40:1697–1721

[22] Moučka R, Kazantseva N, Sapurina I (2018) Electric properties of MnZn ferrite/polyaniline composites: the implication of polyaniline morphology. J Mater Sci 53:1995–2004. https://doi.org/10.1007/s10853-017-1620-6

[23] Dhand C, Das M, Datta M, Malhotra BD (2011) Recent advances in polyaniline based biosensors. Biosens Bioelectron 26:2811–2821

[24] Song E, Choi JW (2013) Conducting polyaniline nanowire and its applications in chemiresistive sensing. Nanomaterials 3:498–523

[25] Salehi MH, Golbaten-Mofrad H, Jafari SH, Goodarzi V, Entezari M, Hashemi M, Zamanlui S (2021) Electrically conductive biocompatible composite aerogel based on nanofibrillated template of bacterial cellulose/polyaniline/nano-clay. Int J Biol Macromol 173:467–480

[26] Pei L, Ma Y, Qiu F, Lin F, Fan C, Ling X (2020) Synthesis of polyaniline/graphene nanocomposites and electrochemical sensing performance for formaldehyde. Curr Anal Chem 16:493–498

[27] Mahmoud ME, Amira MF, Seleim SM, Abouelanwar ME (2021) Behavior of surface coated zirconium silicate-nanopolyaniline with nano zerovalent copper ($ZrSiO_4$@-NPANI@nZVCu) toward catalytic reduction of nitroanilines. Mater Chem Phys 258:123890

[28] Zhang Y, Ma Y, Wei T, Lin FF, Qiu FL, Pei LZ (2018) Polyaniline/zinc bismuthate nanocomposites for the enhanced electrochemical performance of the determination of L-Cysteine. Measurement 128:55–62

[29] Pippara RK, Chauhan PS, Yadav A, Kishnani V, Gupta A (2021) Room temperature hydrogen sensing with polyaniline/SnO_2/Pd nanocomposites. Micro Nano Eng 12:100086

[30] Fan Z, Sun L, Wu S, Liu C, Wang M, Xu J, Tong Z (2019) Preparation of manganese porphyrin/niobium tungstate nanocomposites for enhanced electrochemical detection of nitrite. J Mater Sci 54:10204–10216. https://doi.org/10.1007/s10853-019-03526-4

[31] Ma J, Zhang Z, Yang M, Wu Y, Feng X, Liu L, Tong Z (2016) Intercalated methylene blue between calcium niobate nanosheets by ESD technique for electrocatalytic oxidation of ascorbic acid. Micropor Mesopor Mat 22:123–127

[32] Zhang X, Liu L, Ma J, Yang X, Xu X, Tong Z (2013) A novel metalloporphyrin intercalated layered niobate as an electrode modified material for detection of hydrogen peroxide. Mater Lett 95:21–24

[33] Lee YR, Kim IY, Kim TW, Lee JM, Hwang SJ (2012) Mixed colloidal suspensions of reduced graphene oxide and layered metal oxide nanosheets: useful precursors for the porous nanocomposites and hybrid films of graphene/metal oxide. Chem Eur J 18:2263–2271

[34] Kawaguchi T, Horigane K, Itoh Y, Kobayashi K, Horie R, Kambe T, Akimitsu J (2018) Crystal structure and superconducting properties of $KSr_2Nb_3O_{10}$. Physica B 536:830–832

[35] Lee WH, Im M, Kweon SH, Woo JU, Nahm S, Choi JW, Hwang SJ (2017) Synthesis of $Sr_2Nb_3O_{10}$ nanosheets and their application for growth of thin film using an electrophoretic method. J Am Ceram Soc 100:1098–1107

[36] Yoshimoto S, Ohashi F, Kameyama T (2005) Characterization and thermal degradation studies on polyaniline-intercalated montmorillonite nanocomposites prepared by a

solvent-free mechanochemical route. J Polym Sci Pol Phys 43:2705–2714

[37] Ma J, Zhang X, Yan C, Tong Z, Inoue H (2008) Synthesis and characterization of a polyaniline/$HTiNbO_5$ lamellar hybrid nanocomposite. J Mater Sci 43:5534–5539. https://doi.org/10.1007/s10853-008-2837-1

[38] Ma J, Yang M, Chen Y, Liu L, Zhang X, Wang M, Zhang D, Tong Z (2015) Sandwich-structured composite from the direct coassembly of layered titanate nanosheets and Mn porphyrin and its electrocatalytic performance for nitrite oxidation. Mater Lett 150:122–125. https://doi.org/10.1016/j.matlet.2015.03.039

[39] Graf D, Queralto A, Lepcha A, Appel L, Frank M, Mathur S (2020) Electrospun $SrNb_2O_6$ photoanodes from single-source precursors for photoelectrochemical water splitting. Sol Energ Mat Sol C 210:110485

[40] Ding Y, Luo D, Huang Y, Rong B, Chen X, Wei Y, Wu J (2021) Microwave-mechanochemistry-assisted synthesis of Z-scheme $HSr_2Nb_3O_{10}/WO_3$ heterojunctions for improved simulated sunlight driven photocatalytic activity. J Environ Chem Eng 9:104624

[41] Patel BR, Noroozifar M, Kerman K (2020) Prussian blue-doped nanosized polyaniline for electrochemical detection of benzenediol isomers. Anal Bioanal Chem 412:1769–1784

[42] Pan B, Xu J, Zhang X, Li J, Wang M, Ma J, Tong Z (2018) Electrostatic self-assembly behavior of exfoliated $Sr_2Nb_3O_{10}^-$ nanosheets and cobalt porphyrins: exploration of non-noble electro-catalysts towards hydrazine hydrate oxidation. J Mater Sci 53:6494–6504. https://doi.org/10.1007/s10853-018-2033-x

[43] Yan X, Chen J, Yang J, Xue Q, Miele P (2010) Fabrication of free-standing, electrochemically active, and biocompatible graphene oxide-polyaniline and graphene-polyaniline hybrid papers. ACS Appl Mater Interfaces 2:2521–2529

[44] Lee D, Char K (2002) Thermal degradation behavior of polyaniline in polyaniline/Na^+-montmorillonite nanocomposites. Polym Degrad Stabil 75:555–560

[45] Rao H, Liu Y, Zhong J, Zhang Z, Zhao X, Liu X, Wang Y (2017) Gold nanoparticle/chitosan@N S co-doped multi-walled carbon nanotubes sensor: fabrication, characterization, and electrochemical detection of catechol and nitrite. ACS Sustain Chem Eng 5:10926–10939

[46] Wang YG, Li HQ, Xia YY (2006) Ordered whiskerlike polyaniline grown on the surface of mesoporous carbon and its electrochemical capacitance performance. Adv Mater 18:2619–2623

[47] Yuan X, Yuan D, Zeng F, Zou W, Tzorbatzoglou F, Tsiakaras P, Wang Y (2013) Preparation of graphitic mesoporous carbon for the simultaneous detection of hydroquinone and catechol. Appl Catal B Environ 129:367–374

[48] Feng X, Shi Y, Hu Z (2011) Polyaniline/polysulfone composite film electrode for simultaneous determination of hydroquinone and catechol. Mater Chem Phys 131:72–76

[49] Sudhakara SM, Devendrachari MC, Kotresh HMN, Khan F (2021) Silver nanoparticles decorated phthalocyanine doped polyaniline for the simultaneous electrochemical detection of hydroquinone and catechol. J Electroanal Chem 884:115071

[50] Hu F, Chen S, Wang C, Yuan R, Yuan D, Wang C (2012) Study on the application of reduced graphene oxide and multiwall carbon nanotubes hybrid materials for simultaneous determination of catechol hydroquinone, p-cresol and nitrite. Anal Chim Acta 724:40–46

[51] Sadeghi S, Fooladi E, Malekaneh M (2015) A new amperometric biosensor based on Fe_3O_4/polyaniline/laccase/chitosan biocomposite-modified carbon paste electrode for determination of catechol in tea leaves. Appl Biochem Biotech 175:1603–1616

[52] Song Y, Zhao M, Wang X, Qu H, Liu Y, Chen S (2019) Simultaneous electrochemical determination of catechol and hydroquinone in seawater using Co_3O_4/MWCNTs/GCE. Mater Chem Phys 234:217–223

[53] Guo HL, Peng S, Xu JH, Zhao YQ, Kang X (2014) Highly stable pyridinic nitrogen doped graphene modified electrode in simultaneous determination of hydroquinone and catechol. Sensor Actuat B Chem 193:623–629

[54] Chen Y, Liu X, Zhang S, Yang L, Liu M, Zhang Y, Yao S (2017) Ultrasensitive and simultaneous detection of hydroquinone, catechol and resorcinol based on the electrochemical co-reduction prepared Au-Pd nanoflower/reduced graphene oxide nanocomposite. Electrochim Acta 231:677–685

[55] Huang YH, Chen JH, Ling LJ, Su ZB, Sun X, Hu SR, San He Y (2015) Simultaneous electrochemical detection of catechol and hydroquinone based on gold nanoparticles@carbon nanocages modified electrode. Analyst 140:7939–7947